

# Rolled-up Functionalized Nanomembranes as Three-Dimensional Cavities for Single Cell Studies

Wang Xi,<sup>†,‡</sup> Christine K. Schmidt,<sup>\*,§</sup> Samuel Sanchez,<sup>\*,†,‡</sup> David H. Gracias,<sup>||</sup> Rafael E. Carazo-Salas,<sup>§</sup> Stephen P. Jackson,<sup>§,⊥</sup> and Oliver G. Schmidt<sup>†,¶,■</sup>

<sup>†</sup>Institute for Integrative Nanosciences, IFW Dresden, Helmholtzstrasse 20, D-01069 Dresden, Germany

<sup>‡</sup>Max Planck Institute for Intelligent Systems, Heisenbergstrasse 3, 70569 Stuttgart, Germany

<sup>\*</sup>The Gurdon Institute and Departments of Biochemistry and Genetics, University of Cambridge, Tennis Court Road, Cambridge CB2 1QN, United Kingdom

<sup>||</sup>Department of Chemical and Biomolecular Engineering, Johns Hopkins University, Baltimore, Maryland 21218, United States

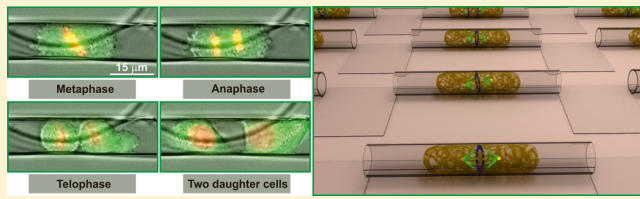
<sup>⊥</sup>The Wellcome Trust Sanger Institute, Hinxton, Cambridge, CB10 1SA, United Kingdom

<sup>¶</sup>Material Systems for Nanoelectronics, Chemnitz University of Technology, Reichenhainer Strasse 70, D-09107 Chemnitz, Germany

<sup>■</sup>Center for Advancing Electronics Dresden, Dresden University of Technology, Georg-Schumann-Str. 11, 01187 Dresden, Germany

## Supporting Information

**ABSTRACT:** We use micropatterning and strain engineering to encapsulate single living mammalian cells into transparent tubular architectures consisting of three-dimensional (3D) rolled-up nanomembranes. By using optical microscopy, we demonstrate that these structures are suitable for the scrutiny of cellular dynamics within confined 3D-microenvironments. We show that spatial confinement of mitotic mammalian cells inside tubular architectures can perturb metaphase plate formation, delay mitotic progression, and cause chromosomal instability in both a transformed and nontransformed human cell line. These findings could provide important clues into how spatial constraints dictate cellular behavior and function.



**KEYWORDS:** *Nanomembranes, rolled-up nanotechnology, mitosis, 3D cell culture scaffold, spatial confinement, chromosome segregation errors*

Cell biology studies often use mammalian cells cultured on conventional two-dimensional (2D) substrates, such as Petri dishes and patterned planar substrates. However, many cellular processes happen in spatially confined physiological environments encompassing a plethora of external physical and chemical cues that contribute to the life cycle of a cell, including its proliferation,<sup>1–3</sup> growth,<sup>4,5</sup> apoptosis,<sup>6–8</sup> and differentiation.<sup>9–11</sup> For instance, transformed cells inside primary tumors are subjected to high levels of spatial and mechanical confinement due to enhanced extracellular matrix stiffness, elevated hydrostatic pressure, and increased cell density.<sup>12</sup> Increased spatial constrictions are also predominant features during cancer metastasis, when disseminated tumor cells, which are much larger than lymphatic or other blood cells and often contain higher ploidies, circulate the vascular system through narrow capillaries with diameters often smaller than half their own size,<sup>13</sup> where they may proliferate intravascularly under spatial constraints comparable to the situations inside microcavities.<sup>14–16</sup> To gain insights into mitotic pathways occurring in such three-dimensional (3D) environments, we developed a microtubular platform to investigate the division of mammalian cells exposed to the capillary confinement of our microtubes

(see Note on three dimensionality of cavities in Supporting Information).

Recently, the importance of physical cues, such as the geometry, spatial confinement, and adhesiveness of cell culture substrates, for various cell behaviors has been demonstrated. It has, for instance, been revealed that the geometric shape of 2D cell adhesive surfaces affects mitosis,<sup>3,17</sup> a mechanical process with intrinsic 3D spatial requirements. Thus, spatial confinement can influence the orientation of the spindle machinery, which is critical for the fate of daughter cells by determining their future spatial positioning. Stringent confinement of dividing human cells on 2D substrates along a single vertical axis can lead to a high percentage of multipolar cell divisions,<sup>18,19</sup> which are both abnormal and often lethal.<sup>20</sup> While these observations point to essential roles for cell adhesion geometry and spatial confinement in controlling mitosis in cells cultured on 2D substrates, the effects of 3D microenvironments on cell division are just starting to be unveiled.<sup>21</sup> Furthermore, stringent spatial constraints on cells

**Received:** November 17, 2013

**Revised:** February 24, 2014

**Published:** March 5, 2014

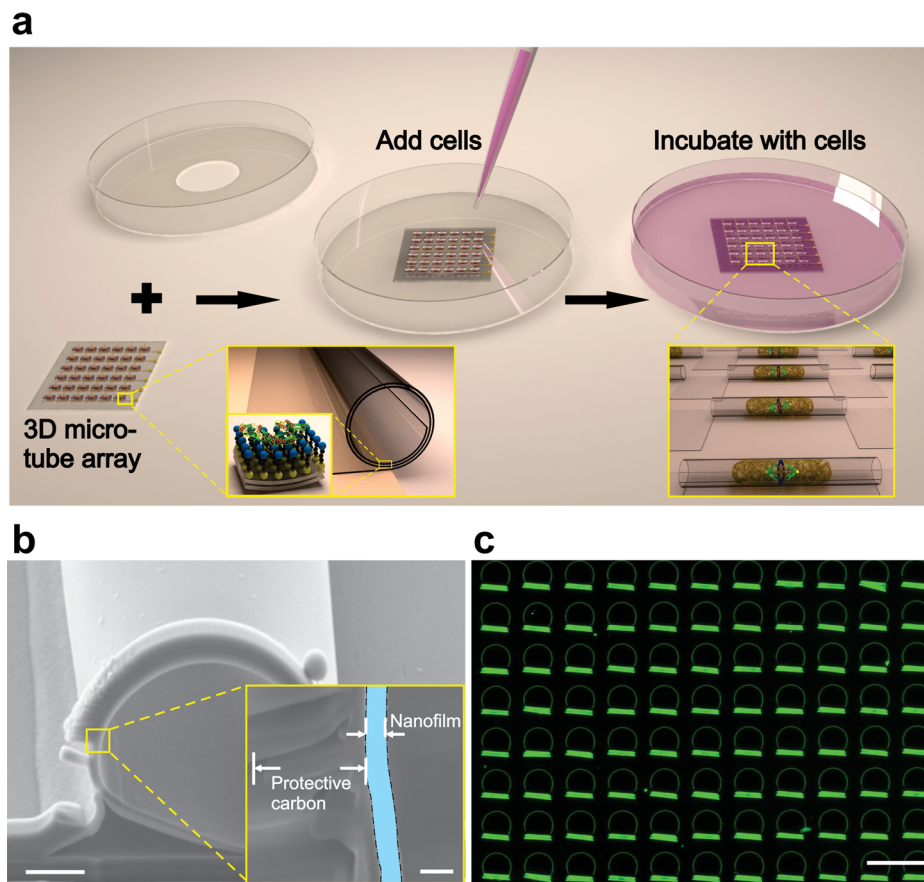


**Figure 1.** A versatile 3D cell assay platform to image mammalian cell behavior in living cells under spatial confinement and in high resolution. (a) Schematic depicting the 3D tubular platform array cocultured with living cells for studying single cell behaviors. The zoomed-in image in the bottom left shows the rolled-up nanotechnology fabrication of transparent SiO/SiO<sub>2</sub> microcavities on a transparent substrate. The insert indicates that the surface of the microcavities was biofunctionalized with a self-assembled monolayer of octadecylphosphonic acid, yellow, brown and blue spheres, to which fibronectin (on top of blue spheres) was covalently coupled. The zoomed-in figure in the bottom right shows the encapsulation of individual proliferating cells inside the microcavities. The transparent platform is suitable for high-resolution microscopy imaging. (b) SEM images of the cross-section of a typical microcavity. The rolled-up nanomembrane with a thickness <100 nm is revealed through a focused ion beam cut. (c) Fibronectin-functionalized rolled-up microcavity array mimics aspects of the chemical *in vivo* environment of cells inside tissues. The green immunofluorescent staining of fibronectin confirms the conjugation of this extracellular matrix protein to the microcavity surfaces. Scale bars, 2 μm, 100 nm, and 100 μm in (b), (b) inset, and (c), respectively.

dividing in 3D adhesive microtube structures, which are common within and around tissues, remain largely unknown. The development of novel methods, which mimic the 3D nature of tissues, is therefore crucial to uncover the influences of spatial constraints on cell division in 3D contexts. Moreover, defined ways of manipulating and monitoring cellular microenvironments are required to unravel the specific effects that spatial constraints exert on dividing cells. Several studies have contributed to the fabrication of 3D cavities for cell culture,<sup>22–28</sup> but to our knowledge, herein, we provide the first detailed investigation of mammalian single cell divisions under tubular confinement. In comparison to our approach, prior work either focused on nonadherent simpler eukaryotic cells,<sup>22</sup> employed nontransparent materials with questionable biocompatibility,<sup>24,28</sup> or used large diameter rolls not suitable for single cell encapsulation and high-resolution optical imaging.<sup>26,27</sup> Our tubular system offers a novel platform that serves as a tissue culture scaffold in 3D, while allowing only one-dimensional freedom for cell growth.

Here, we use nanopatterning and strain engineering, the latter being based on generating differential strain (or vertical strain gradients) in nanomembranes,<sup>29</sup> to establish a 3D single

cell cavity platform. This platform allows the noninvasive encapsulation of different types of individual mammalian cells, such as transformed HeLa cancer cells and nontransformed retinal pigment epithelial (RPE1) cells, within transparent biofunctionalized microcavities of varying diameters. The cavities are made of transparent nanomembranes that overcome the problems of reflection and refraction of light traveling through the layers and are functionalized with self-assembled monolayers of biomolecules to mimic *in vivo* conditions. Through using this platform, we are able to deform rounded-up mitotic cells into elongated cylinder shapes, morphologies that are difficult to generate via molecular genetic tools or other micromanipulations on 2D substrates. Moreover, by analyzing cell behavior under such 3D culture conditions, we have uncovered a strong positive correlation between the extent of confinement and the occurrence of chromosome segregation errors (CSEs), which is a hallmark of many cancer cells. This increase in genomic instability occurs despite prolonged activation of the spindle assembly checkpoint. Collectively, our findings may help to reveal the *in vivo* cellular processes that happen under physiological conditions of 3D physical confinement.

Figure 1a shows arrays of on-chip microcavities inside which individual proliferating cells can be entrapped. To generate this 3D cell culturing system, we deposited SiO/SiO<sub>2</sub> nanofilms that were self-folded into microcavities on a transparent substrate. We then mass-produced the tubes as arrays with highly defined and scalable diameters<sup>22,29</sup> (Figure 1a, see Methods in Supporting Information for further details). The lengths of the cavities can be tailored from 100 μm for accommodation of a single cell to 1 mm to contain clusters of cells. We used lengths of 100 μm to enrich for cavities containing single cells in order to minimize any effects due to potential cell–cell contact inhibition. These SiO/SiO<sub>2</sub> nanofilms usually have a thickness of less than 100 nm (Figure 1b), which offers high transparency and excellent optical properties,<sup>30–32</sup> making them suitable for observation with high- and super-resolution microscopes. To mimic aspects of the chemical environment of mammalian cells *in vivo*, we used specialized surface chemistry to biofunctionalize the cavities with fibronectin, a major extracellular matrix component<sup>33</sup> (Figure 1a, inset of zoomed-in image on the bottom left and Figure 1c). Notably, this platform overcomes drawbacks of conventional polydimethylsiloxane (PDMS) microchannel methods, such as migration of incomplete reticulated PDMS within the channel and adsorption of added active molecules that could bias results.<sup>34</sup> Moreover, the rolled-up cavities contain smooth internal surfaces (Figure 1a,b) without the sharp edges that are common in conventional rectangular microchannels fabricated via etching processes.

Two immortal adherent human cell lines were chosen for this study: transformed HeLa cells, a cell line derived from human cervical cancer, and RPE1 cells as a nontransformed cell line. Both of the cell lines are known to regulate their cellular behaviors according to the extent of geometric confinement,<sup>3,35</sup> but HeLa cells having a 3N+ karyotype of approximately 82 chromosomes,<sup>36</sup> compared to a diploid karyotype of 46 chromosomes in RPE1 cells, might lead to differences in the way these two cells respond to spatial confinement. To encapsulate individual cells inside the microcavities, we added 3 mL cell suspensions containing  $\sim 2 \times 10^5$  cells/mL to the platform inside a 35 mm diameter Petri dish, followed by a 30 min incubation with shaking at 37 °C. During the next 24 h, some cells spontaneously migrated into the cavities (Figure 2a), as monitored by optical live-cell imaging and illustrated by scanning electron microscopy of cells entrapped in close proximity to the apertures of the cavities (Figure 2a,b, respectively). These images also revealed that in contrast to 2D substrates tubular confinement prevented cells from extensive spreading but enabled them to adapt a column-like cell shape.

We used tubular arrays containing a set number of around 500 cavities in 1 cm<sup>2</sup> per chip and thus the percentage of cavities containing cells at a defined time point reflected the tendency of different cell types to migrate into and remain inside the scaffolds, as shown in Figure 2c. By systematically tuning cavity diameters from 4 to 18 μm, we found that the number of RPE1 cells contained within cavities sharply decreased once diameters were reduced to <10 μm (~8% in ≤10 μm versus ~35% in ≥10 μm cavities, Figure 2c). By contrast, HeLa cells were observed in more than 40% of the cavities with diameters between 7 and 9 μm and were almost twice as likely to be found inside cavities of 4–6 μm in diameter, a size range representing only around 25% of their rounded-up diameters ( $20.9 \pm 1.0$  μm,  $n = 23$ , for HeLa cells

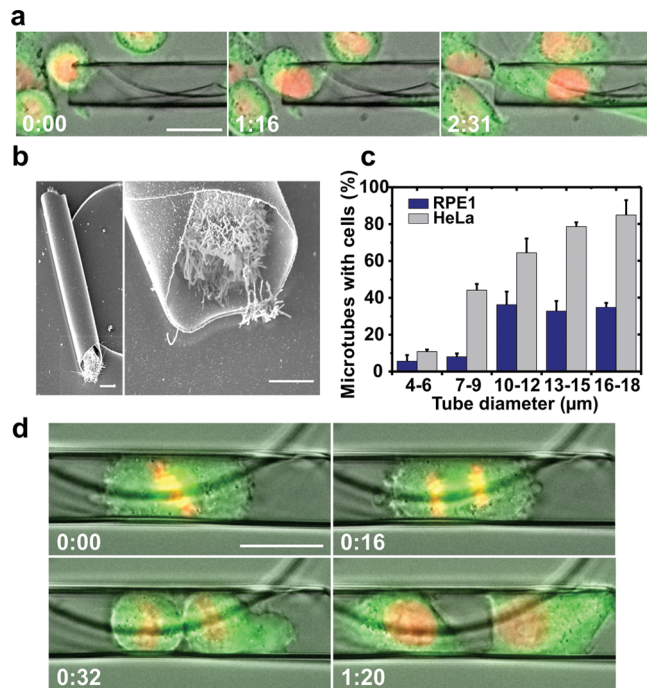


**Figure 2.** The encapsulation of individual mammalian cells and the visualization of their cell division process inside rolled-up microcavities. (a) Time-lapse images (merged phase-contrast and fluorescent) of HeLa cells coexpressing histone H2B-mCherry (red) and GFP-tubulin (green) illustrating the migration of a cell into an ~14 μm microcavity. (b) SEM images of HeLa cells inside a microcavity. (c) The percentage of microcavities containing at least one cell (RPE1 or HeLa) after 24 h incubation. Samples containing ~500 microcavities in 1 cm<sup>2</sup> were used for the analysis. The average percentage was calculated from ≥2 samples in each case. (d) Fluorescent and phase-contrast time-lapse images of an entrapped dividing HeLa cell (GFP-tubulin, green; H2B-mCherry, red). Scale bars, 15 μm in (a,d), 5 μm in (b); time in hour/min format.

and  $19.6 \pm 1.1$  μm,  $n = 25$ , for RPE1 cells). These findings suggest that HeLa cells might have a stronger capacity than RPE1 cells to migrate into and/or remain inside narrow <10 μm tubular structures. As RPE1 cells tend to spread prior to migration,<sup>37</sup> this increase in size might make it more difficult for this cell line to migrate into the cavities. Above 9 μm cavity diameters, most encapsulated cells of both cell lines were able to divide inside the tubular confinement, highlighting the general biocompatibility of our platform (a representative HeLa cell division is shown in Figure 2d). Importantly, the entrapped cells remaining inside the cavities for extended time periods continued to proliferate for at least two additional cell cycles (as long as our observation periods lasted), indicating no major defects in nutrient or gas exchange between the encapsulated cells and the culture medium (see Videos 1a and b (si\_002 and si\_003) in Supporting Information).

We use GFP-tubulin and histone H2B-mCherry expressing HeLa cells for live-cell imaging, which allows us to visualize the different stages of mitosis based on the transformation in chromosome and spindle morphology (Figure 3a–c and see Videos 2a–c (si\_004–si\_006) in Supporting Information). In most cases of unconfined cells grown on 2D-substrates (henceforth termed free cells), the chromosomes are quickly aligned between the separated spindle poles after nuclear envelope breakdown (NEB) and form a metaphase plate (Figure 3a). Within 40 min, the cells then proceed through

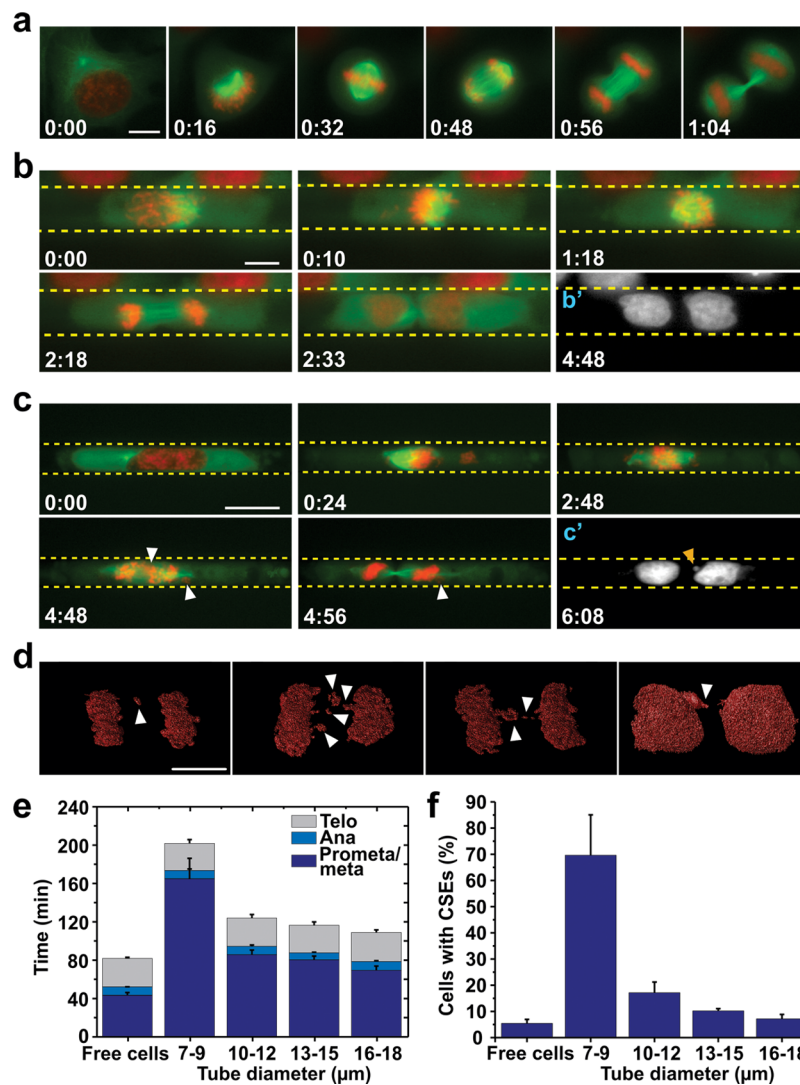


**Figure 3.** Spatial confinement leads to mitotic delays in prometa-/metaphase and chromosome segregation errors (CSEs). (a) Representative time-lapse z-stack projections of a free dividing HeLa cell coexpressing GFP-tubulin (green) and H2B-mCherry (red). (b,c) As (a) but for cells dividing in 13 μm (b) and 9 μm (c) microcavities, respectively. Note the presence of CSEs highlighted by white arrowheads in (c) and the subsequent formation of micronuclei in the arising daughter cells (orange arrowhead in c'). In contrast, no obvious micronuclei (b') formed after accurate segregation of chromosomes in (b). (d) the 3D reconstructions of CSEs (arrowheads) in anaphase HeLa cells cultured in 3D tubular spatial confinement. (e) Quantification of the mean durations of different mitotic phases ( $\pm$ SD) in HeLa cells ( $n = 86, 31, 40, 25$ , and  $11$  from left to right), starting from the beginning of cell rounding and nuclear envelope breakdown to the maximum visible contractile ring constriction between the two daughter cells. (f) Histogram showing the mean percentages ( $\pm$ SD) of anaphase cells with CSEs ( $n = 355, 35, 61, 53, 106$  from left to right). Scale bars, 10 μm, time in hour/min format.

metaphase and accurately segregate their chromosomes into two daughter cells in anaphase.

Two examples of HeLa cell divisions inside microcavities are presented in Figure 3b,c (13 and 9 μm tube diameter, respectively). We observed that the physical confinement of the cavities perturbed the chromosome arrangement after NEB and often lead to poorly aligned metaphase plates; in the extreme cases of <10 μm microcavities, the chromosomes remained disordered throughout prometa-/metaphase (Figure 3c). Thus, instead of well-defined metaphase plates, the majority of chromosomes often accumulated in a disordered manner near the center of the spindle. Furthermore, we commonly detected noncongressed chromosomes that persisted proximal to the poles throughout prometa-/metaphase (indicated by white arrowheads in Figure 3c). These findings demonstrated that physical confinement inside 3D-microcavities significantly

compromises the alignment of chromosomes into a metaphase plate. It is worth emphasizing here that the cells “voluntarily” engage with such microenvironments (Figure 2a). As a prerequisite for accurate chromosome segregation, these aberrations in chromosome arrangements might undermine genomic stability. Indeed, super-resolution images of HeLa cells in late anaphase to telophase within microcavities often show lagging chromosomes (Figure 3d, and Supporting Information Figure S1), as judged by the presence of chromosomes in the center of anaphase spindles that were delayed in their movements toward spindle poles at least until the onset of telophase. These noncongressed and/or lagging chromosomes in anaphase, collectively referred to as chromosome segregation errors (CSEs) henceforth, almost always (90%,  $n = 20$ ) resulted in at least one daughter cell containing a readily detectable micronucleus (Figure 3c'). In contrast, in daughter cells after

accurate chromosome splitting no such obvious micronuclei could be observed (Figure 3b'). This indicates a strong correlation between micronuclei in these cells and preoccurred chromosome missegregation events, as reported previously.<sup>38</sup> Such errors in chromosome segregation have been recognized as a direct driving force of tumorigenesis<sup>39</sup> and are strictly controlled by the spindle assembly checkpoint (SAC), a well-established genome maintenance mechanism that senses the attachment and tension of sister-kinetochores and prevents progression to anaphase until bipolar attachment of kinetochores is achieved.<sup>40</sup> Consistent with our observations, once trapped into microcavities  $<18\ \mu\text{m}$  (86% of the diameter of rounded-up mitotic HeLa cells), cells divided with strongly pronounced prometa-/metaphase delays ranging from  $\sim 70$  to  $\sim 160$  min under various spatial confinement (from 18 to  $7\ \mu\text{m}$ , respectively), while the other mitotic phases were comparable in length between free and confined cells (Figure 3e). Strikingly, in some cases prometa-/metaphase lasted for  $>5$  h whereas the maximum durations we observed in unconfined cells did not exceed 60 min.

To test whether the SAC was the cause of the extended prometa-/metaphase delays described above, we added reversine, an inhibitor of the SAC kinase MPS1,<sup>41</sup> to our 3D cell culture platform. We found that SAC inhibition entirely reversed the prometa-/metaphase delays in HeLa cells inside all microcavity diameter ranges tested (see examples in Supporting Information Figure S2a,b; compare quantifications in the presence of reversine in Supporting Information Figure S2c with data obtained in its absence in Figure 3e; also see Videos 3a,b (si\_007 and si\_008) in Supporting Information). These findings demonstrated that the prometa-/metaphase delays in spatially confined mitoses reflected a prolonged activation of the SAC and further showed that our 3D cell culture platform permits good permeability and quick diffusion of active small-molecules to the cells trapped inside. This proof-of-concept experiment demonstrates that our platform has great potential for future high-throughput applications such as drug screening or large-scale siRNA depletion studies. Moreover, in the presence of reversine, distinct noncongressed and lagging chromosomes were visible throughout the whole duration of mitosis (Supporting Information Figure S2a,b), resulting in significant increases in chromosome missegregation rates in both spatially confined and free cells (Supporting Information Figure S2d). Accordingly, micronuclei were readily detectable in the arising daughter cells (Supporting Information Figure S2a',b'). We conclude that the presence of micronuclei is tightly linked to chromosome missegregation events in HeLa cells. In the absence of reversine, only  $\sim 5\%$  of free control HeLa cells displayed CSEs in anaphase, whereas under extreme confinement ( $<10\ \mu\text{m}$  cavities), we detected an unprecedented  $>10$ -fold increase ( $\sim 70\%$ ) of anaphase cells with CSEs (Figure 3f). We also observed elevated chromosome missegregation rates of  $\sim 17$ ,  $\sim 10$ , and  $7\%$  in intermediately confined  $10\text{--}12$ ,  $13\text{--}15$ , and  $16\text{--}18\ \mu\text{m}$  microcavities, respectively, which were statistically significant for  $<16\ \mu\text{m}$  microcavities (Figure 3f,  $p$ -value  $<0.005$ ). These data allowed us to determine  $10\ \mu\text{m}$  as a critical lower cylindrical section diameter below which chromosome segregation was impaired in the majority of 3D-cultured HeLa cells (Figure 3f). Among the cells with CSEs, around 30% ( $n = 46$ , all of them in microcavities  $<10\ \mu\text{m}$ ) proceeded into anaphase before chromosome congression was completed. It remains unclear how exactly cells escape the SAC and enter and progress through anaphase. It has been recently

demonstrated by Itabashi et al. that by applying directional mechanical compression to mitotic spindles one can accelerate anaphase onset.<sup>42</sup> With our tubular confinement approach, we routinely observed that mitotic spindles rotate until they align along the long axis of the microtubes. Only then do the cells enter anaphase (data not shown). One possibility is that when the spatial constriction is perpendicular to the spindle axis (as is the case when spindles are aligned along the long axes of the microtubes) the tension generated within the spindle may trigger chromosome segregation<sup>42</sup> even if the SAC might still be active.

Abnormal cell divisions have been previously reported under spatial confinement in cells cultured on 2D substrates.<sup>18,19</sup> In these studies, the authors applied pressures to mammalian cells in a single vertical axis, which deformed mitotic cells into enlarged flattened discoid cell shapes, causing a failure of spindle morphogenesis and loss of chromosomes from the nascent spindle due to the limited reach of microtubules ( $\sim 15\ \mu\text{m}$  in the length). Although mechanical compression is known to regulate mitotic spindle mechanics, such as spindle widening and elongation,<sup>43</sup> a large proportion of HeLa cells under extreme planar confinement undergoes irreversible pole splitting, which can lead to lethal multipolar cell divisions.<sup>18\text{--}20</sup>

In our tubular confinement conditions, although some chromosomes localized also close to the centrosomes, away from the metaphase plate (Figure 3c), pole splitting never occurred and neither did multipolar cell divisions, demonstrating that pole splitting is not the primary cause for the CSEs observed in our system and that the single or multiple lagging/uncongressed chromosomes occurring in the presence of bipolar anaphase spindles in our system must be caused by different mechanisms (Figure 3d and Supporting Information Figure S1). Such differences with 2D systems might be the result of tubular confinement allowing only one-dimensional geometric freedom, which may help to preserve a morphologically normal spindle with regards to its polarity. Thus, while the previous method is based on 1D confinement (from the top only), our tubular confinement system imposes spatial constraints in two dimensions (from the top and the sides). Hence, one could envision that 1D confinement may not constrict the metaphase plate initially, as they might still form properly if aligned in parallel to the culture dish surface.<sup>44</sup> By contrast, metaphase plates forming inside microcavities cannot evade spatial confinement in any orientation in space. This difference in confinement may also explain why the majority of asymmetric cell divisions/mitotic delays in 1D confinement were mainly observed in extremely narrow gaps  $\leq 5\text{--}7\ \mu\text{m}$ ,<sup>18,19</sup> which are around 25% of the rounded-up mitotic cell diameter ( $\sim 20\ \mu\text{m}$ ) and close to the height of spread-out interphase cells; such dimensions are well below the value of  $18\ \mu\text{m}$ , below which we observed mitotic delays and chromosome arrangement perturbations in 3D-cultured cells dividing in our 2D-confined microenvironments. Furthermore, our tubular confinement may also have an impact on other mitotic machineries and processes, such as the formation of chromosome rosettes, prometaphase structures that have recently been identified as crucial structures facilitating spindle assembly,<sup>44</sup> and centrosome separation kinetics during spindle maturation. It will thus be of high interest to investigate in future experiments how exactly physical constraints affect spindle kinetics.

The influences of tubular confinement on nontransformed RPE1 cell divisions were also significant, especially inside  $<10\ \mu\text{m}$  microcavities (Supporting Information Figure S3). In

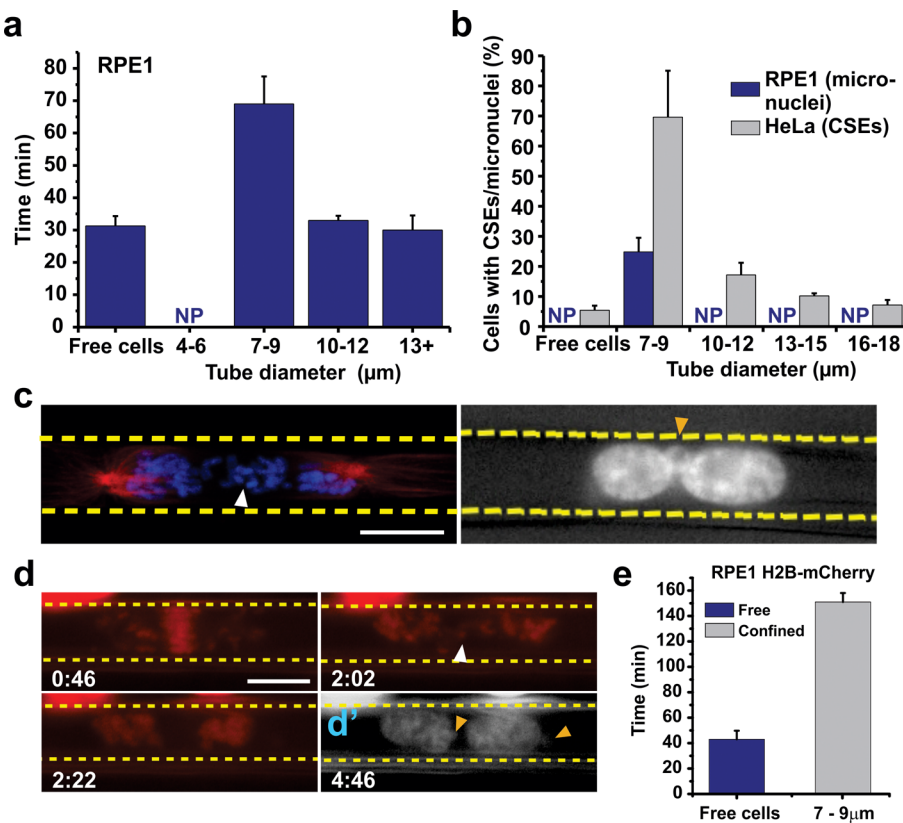


**Figure 4.** Tubular confinement affects RPE1 cell division. (a) Quantification of the mean mitotic durations ( $\pm$ SD) of free and confined untagged RPE1 cells ( $n = 65$ , NP (not present), 11, 12, 17 from left to right) as judged from the beginning of cell rounding and nuclear envelope breakdown to the maximum visible contractile ring constriction between the two daughter cells. (b) Histogram of the mean percentages ( $\pm$ SD) of RPE1 cells containing micronuclei after telophase ( $n = 93$ , 16, 22, 11, 10 from left to right, blue). CSEs in HeLa anaphase cells (as in Figure 3f) are shown as a reference (gray bars). (c) The 3D-projected fluorescent images (anti- $\alpha$ -tubulin, red; chromosomes, DAPI, blue) of an anaphase RPE1 cell (left) with lagging chromosomes (white arrowhead) and an example of a daughter cell containing a micronucleus after telophase (right, orange arrowhead). (d) Representative time-lapse z-stack projections of a dividing RPE1 cell stably expressing histone H2B-mCherry (red). Note the presence of CSEs highlighted by a white arrowhead and the micronuclei formed in both daughter cells (d', orange arrowheads). (e) As (a) but for RPE1 cells stably expressing H2B-mCherry ( $n = 15$  and 4 from left to right). Scale bars, 10  $\mu\text{m}$ , time in hour:min format.

contrast to HeLa cells – the majority of which still entered and progressed through mitosis when entrapped in such microcavities (Supporting Information Figure S4 left) – the extreme tubular confinement of these microcavities often prevented RPE1 cells from entering mitosis and frequently led to their death (judged by the absence of cell motion eventually followed by cell disintegration; Figure S4 right and see Video 4 (si\_009) in Supporting Information). In microcavities between 7 to 9  $\mu\text{m}$ , only around 30% of RPE1 cells progressed through mitosis, and they did so with a >2-fold prolonged duration compared to free cells or cells in larger microcavities (Supporting Information Figure S3c and Figure 4a and see Video 5 (si\_010) in Supporting Information). This highlighted 10  $\mu\text{m}$  as a critical cylindrical section diameter for RPE1 cell division. Furthermore, we found that the key phenomenon of chromosome segregation errors in HeLa cells (Figure 3c',d) seemed to be conserved in the nontransformed RPE1 cell line (Figure 4b,c). RPE1 cells remained highly mobile within the tubes and the majority escaped the fields-of-view during time-lapse imaging experiments. Because of these technical difficulties, we fixed untagged RPE1 cells at a certain time after release from a double-thymidine block to enrich for late anaphase/early telophase cells inside the tubes. Immunofluorescent staining of  $\alpha$ -tubulin and staining with DAPI allowed us to visualize the spindle and DNA, respectively, and quantify the

occurrence of CSEs (Figure 4c, left) and micronuclei (Figure 4c, right), the latter of which are often formed after previously occurred chromosome missegregation events (see above for our findings in HeLa cells and a previous report<sup>38</sup>). Thus, we recorded micronuclei in ~25% of fixed RPE1 cells when these cells divided inside 7–9  $\mu\text{m}$  microcavities (Figure 4b). We also captured histone H2B-mCherry expressing RPE1 cells in live-cell imaging experiments when they were dividing inside <10  $\mu\text{m}$  microcavities (Figure 4d and see Video 6 (si\_011) in Supporting Information). These imaging sequences confirm a prolonged mitotic duration also in RPE1 H2B-mCherry cells (Figure 4e), lagging/uncongressed chromosomes in anaphase (white arrowhead in Figure 4d) and the subsequent formation of micronuclei in daughter cells (orange arrowheads in Figure 4d'). Similarly to untagged RPE1 cells, around 29% of the RPE1 H2B-mCherry cells recorded by live-cell imaging (some videos were recorded just before anaphase onset) showed CSEs and the generation of micronuclei, while the remaining cells underwent chromosome segregation with high fidelity. In the latter cells, no micronuclei were formed in the daughter cells (see video 7 (si\_012) in Supporting Information). These observations point to a tight link in RPE1 cells between micronuclei and previously occurred CSEs. The findings described above show that genomic instability in response to spatial confinement is of a general, rather than a cell-line

specific or cancer-cell specific nature, and that it is not due to histone overexpression. However, unlike the situation with HeLa cells, RPE1 cells showed no signs of gross chromosomal instability in microcavities  $\geq 10 \mu\text{m}$  (Figure 4b and Supporting Information Figure S5), indicating that HeLa and RPE1 cells responded to constrained spatial 3D environments in largely similar fashions but with differences regarding the extent and exact spatial onset of impairments (Supporting Information Figure S4).

In summary, the rolled-up nanomembranes technology presented herein provides a versatile and experimentally convenient way of creating 3D structures of defined geometry for the growth and proliferation of mammalian cells in 3D contexts. We have highlighted the potential of this platform by growing two kinds of human cell lines, HeLa and RPE1, inside the microcavities and applying modern biotechnologies, including live-cell imaging and state-of-the-art high-resolution and super-resolution microscopy, to scrutinize the effects of varying extents of tubular spatial constraints on mammalian cell division in 3D contexts. With this versatile engineered platform, we observed a remarkable correlation between the fidelity of chromosome segregation and spatial confinement, and determined  $10 \mu\text{m}$  as a critical lower cylindrical section diameter for chromosome segregation in the two different 3D-cultured cell lines. Below this threshold, the physical disruptions to cell divisions led to drastic increases of CSEs not only in HeLa cells, an aneuploid cancer cell line, but also in nontransformed diploid human RPE1 cells. Whether the  $10 \mu\text{m}$  threshold directly results from the observed impairments in chromosome arrangement and/or the perturbation to other mitotic kinetics, remains to be determined.

The higher percentage of CSEs and their presence also in larger microcavities in the case of HeLa cells may be due to the increased number of chromosomes present in HeLa cells (around 82 compared to 46 in RPE1 cells), which are likely to require more space in 3D for their metaphase plates and may thus make HeLa cells more vulnerable to the effects of spatial confinement on genome stability. We noticed that, while highly disordered metaphase plates and noncongressed chromosomes were present throughout the whole prometa-/metaphase duration under extreme confinement in both cell lines, some of the HeLa and RPE1 cells could still proceed into anaphase despite HeLa cells harboring an even stronger SAC than RPE1 cells.<sup>45</sup> This might be correlated with the increasing spindle tension upon spatial confinement, which has been reported to accelerate anaphase onset<sup>42</sup> as discussed in detail above. We observed mitotic slippage in 5.2% of HeLa cells and 14% of RPE1 H2B-mCherry cells inside 7–9- $\mu\text{m}$  microcavities. Interestingly, we also observed cell death during mitosis (in metaphase), but only in HeLa cells (15.8% of the HeLa cells dividing inside 7–9- $\mu\text{m}$  microcavities). While extreme confinement prevented RPE1 cells from entering mitosis, most of the HeLa cells still divided inside the microcavities under the same degrees of confinement, a major difference among the otherwise similar phenomena between the two cell lines. Since cancer cells often lose their ability to efficiently activate various checkpoints, including for instance the ones that control mitotic entry,<sup>46,47</sup> this likely reflects the transformed nature of HeLa cells. Our highly parallel assay has the potential to investigate the division of large numbers of single cells in isolation, which can be important to investigate tumor heterogeneity as well as the progression of cancer.<sup>48</sup> Furthermore, in comparison to previously reported 2D

micromanipulation approaches where cells passively react to mechanical stimuli applied to them, in our setup cells “voluntarily” engage with environments posing spatial constraints, leading to detrimental consequences such as genome instability. These observations indicate a possible intrinsic lack of mechanical-sensory checkpoints in mammalian cells that would otherwise prevent them from “self-imposed” engagement with such unfavorable mechanical microenvironments. We speculate that further investigation of these phenomena may shed light on the molecular mechanisms underlying tumorigenesis in 3D contexts.

Finally, we note that our platform could also be combined with various other technologies, such as microelectronic circuits and microfluidic lab-in-a-tube systems,<sup>49</sup> and could be expanded to many other adherent cell types/cell lines to study any cellular responses measurable by fluorescent readouts. The simplicity of mass-fabrication of the microcavities as on-chip arrays, together with the spontaneous migration of mammalian cells into the microcavities, might also provide a versatile method suitable for cell invasion experiments to explore fundamental aspects of cell biology relating to metastasis or wound healing, tissue engineering, and drug discovery and development.

## ■ ASSOCIATED CONTENT

### **S Supporting Information**

A description of the detailed fabrication and characterization methods, the materials used, the surface functionalization, and cell culture protocols and procedures for live-cell imaging, drug treatment, and immunofluorescent staining. High-resolution fluorescent images of HeLa cells in ana-/telophase entrapped in microcavities with CSEs are shown. Time-lapse phase contrast images of RPE1 cells undergoing mitosis under different confined situations are presented. Images of DAPI stained anaphase RPE1 cells in various confinements from free cells to 10  $\mu\text{m}$  cavities without CSEs are demonstrated. Videos of HeLa and RPE1 cell behaviors under various confined situations are included. This material is available free of charge via the Internet at <http://pubs.acs.org>.

## ■ AUTHOR INFORMATION

### **Corresponding Authors**

\*E-mail: (S.S.) sanchez@is.mpg.de.

\*E-mail: (C.K.S.) cs681@cam.ac.uk.

### **Author Contributions**

S.S., C.K.S., and O.G.S. conceived the project, W.X., S.S., and C.K.S. designed the experiments with help from R.E.C.-S. and S.P.J. S.S., C.K.S., and O.G.S. supervised the study with help from R.E.C.-S. and S.P.J. W.X. performed and analyzed all experiments with help from C.K.S. and S.S. D.H.G. provided several ideas, helped with the writing, and contributed to the SEM images. W.X., S.S., and C.K.S. wrote the manuscript. All authors commented on and/or edited the manuscript and figures. All authors have given approval to the final version of the manuscript.

C.K.S. and S.S. contributed equally.

### **Notes**

The authors declare no competing financial interest.

## ■ ACKNOWLEDGMENTS

We thank the Gurdon Institute Imaging Facility for microscopy support, especially Nicola Lawrence for helping to optimize the

conditions for OMX 3D-SIM, Daniel Gerlich for the GFP-tubulin/H2B-mCherry expressing HeLa cells and the RPE1 H2B-mCherry cell line, Jon Pines, Takahiro Matsusaka, and Paola Marco for comments, Tom Misteli for supporting the project initialization, Marlitt Viehrig, Anka Kempe, and Britta Koch for support in cell culture, image analysis, and microcavities preparation, Chenglin Yan and Elliot Smith for support in the experiments, Ronny Engelhard for technical support, Daniel Grimm for support in the clean room facilities, and Adria Sales Ramos and Tabea Mundinger (New Materials and Biosystems Department, Max Planck Institute for Intelligent System, Stuttgart) for fluorescent microscopy support. We thank Ralph Träger for providing 3D schematic diagrams. The research leading to these results has received funding from the European Research Council under the European Union's Seventh Framework Programme (FP7/2007-2013)/ERC Grant Agreement 311529 (S.S.) and the Volkswagen Foundation #86 362 (S.S., W.X. and O.G.S.), the Deutsche Forschungsgemeinschaft through the Research Unit FG 1713 (O.G.S.), a FEBS Return-to-Europe fellowship (C.K.S.), and a European Research Council (ERC) Starting Researcher Grant (R.E.C.-S.; SYSGRO). D.H.G. acknowledges funding from the Alexander von Humboldt Foundation and the U.S. National Science Foundation (Grant CMMI 1200241). Research in the S.P.J. laboratory is funded by Cancer Research U.K., the ERC, and the European Community Seventh Framework Programme (DDResponse) with core infrastructure provided by Cancer Research U.K. and the Wellcome Trust.

## ■ REFERENCES

- (1) Singhvi, R.; Kumar, A.; Lopez, G.; Stephanopoulos, G.; Wang, D.; et al. *Science* **1994**, *264*, 696–698.
- (2) Wu, S.; Liu, X.; Hu, T.; Chu, P. K.; Ho, J. P. Y.; et al. *Nano Lett.* **2008**, *8*, 3803–3808.
- (3) Thery, M.; Racine, V.; Pepin, A.; Piel, M.; Chen, Y.; et al. *Nat. Cell Biol.* **2005**, *7*, 947–953.
- (4) Fan, L.; Feng, C.; Zhao, W.; Qian, L.; Wang, Y.; et al. *Nano Lett.* **2012**, *12*, 3668–3673.
- (5) Patel, S.; Kurpinski, K.; Quigley, R.; Gao, H.; Hsiao, B. S.; et al. *Nano Lett.* **2007**, *7*, 2122–2128.
- (6) Chen, C. S.; Mrksich, M.; Huang, S.; Whitesides, G. M.; Ingber, D. E. *Science* **1997**, *276*, 1425–1428.
- (7) Ranzinger, J.; Krippner-Heidenreich, A.; Haraszti, T.; Bock, E.; Tepperink, J.; et al. *Nano Lett.* **2009**, *9*, 4240–4245.
- (8) Ding, L.; Stilwell, J.; Zhang, T.; Elboudwarej, O.; Jiang, H.; et al. *Nano Lett.* **2005**, *5*, 2448–2464.
- (9) Yim, E. K. F.; Pang, S. W.; Leong, K. W. *Exp. Cell Res.* **2007**, *313*, 1820–1829.
- (10) Lee, M. R.; Kwon, K. W.; Jung, H.; Kim, H. N.; Suh, K. Y.; et al. *Biomaterials* **2010**, *31*, 4360–4366.
- (11) Cheng, Z. A.; Zouani, O. F.; Glinel, K.; Jonas, A. M.; Durrieu, M.-C. *Nano Lett.* **2013**, *13*, 3923–3929.
- (12) Erler, J. T.; Weaver, V. M. *Clin. Exp. Metastasis* **2009**, *26*, 35–49.
- (13) Miles, F. L.; Pruitt, F. L.; van Golen, K. L.; Cooper, C. R. *Clin. Exp. Metastasis* **2008**, *25*, 305–324.
- (14) Al-Mehdi, A. B.; Tozawa, K.; Fisher, A. B.; Shientag, L.; Lee, A.; et al. *Nat. Med.* **2000**, *6*, 100–102.
- (15) Wong, C. W.; Song, C.; Grimes, M. M.; Fu, W. L.; Dewhirst, M. W.; et al. *Am. J. Pathol.* **2002**, *161*, 749–753.
- (16) Yamauchi, K.; Yang, M.; Hayashi, K.; Jiang, P.; Yamamoto, N.; et al. *Cancer Res.* **2008**, *68*, 516–520.
- (17) Thery, M.; Jimenez-Dalmaroni, A.; Racine, V.; Bornens, M.; Julicher, F. *Nature* **2007**, *447*, 493–496.
- (18) Lancaster, O. M.; Le Berre, M.; Dimitracopoulos, A.; Bonazzi, D.; Zlotek-Zlotkiewicz, E.; et al. *Dev. Cell* **2013**, *25*, 270–283.
- (19) Tse, H. T. K.; Weaver, W. M.; Di Carlo, D. *PLoS One* **2012**, *7*, e38986.
- (20) Kwon, M.; Godinho, S. A.; Chandhok, N. S.; Ganem, N. J.; Azioune, A.; et al. *Genes. Dev.* **2008**, *22*, 2189–2203.
- (21) Charnley, M.; Anderegg, F.; Holtackers, R.; Textor, M.; Merald, P. *PLoS One* **2013**, *8*, e66918.
- (22) Huang, G.; Mei, Y.; Thurmer, D. J.; Coric, E.; Schmidt, O. G. *Lab Chip* **2009**, *9*, 263–268.
- (23) Schulze, S.; Huang, G.; Krause, M.; Aubyn, D.; Quiñones, V. A. B.; et al. *Adv. Eng. Mater.* **2010**, *12*, B558–B564.
- (24) Yu, M.; Huang, Y.; Ballweg, J.; Shin, H.; Huang, M.; et al. *ACS Nano* **2011**, *5*, 2447–2457.
- (25) Balzer, E. M.; Tong, Z.; Paul, C. D.; Hung, W.-C.; Stroka, K. M.; et al. *FASEB J.* **2012**, *26*, 4045–4056.
- (26) Yuan, B.; Jin, Y.; Sun, Y.; Wang, D.; Sun, J.; et al. *Adv. Mater.* **2012**, *24*, 890–896.
- (27) Jamal, M.; Kadam, S. S.; Xiao, R.; Jivan, F.; Onn, T.-M.; et al. *Adv. Healthcare Mater.* **2013**, *2*, 1066–1066.
- (28) Bausch, C. S.; Koitmäe, A.; Stava, E.; Price, A.; Resto, P. J.; et al. *Appl. Phys. Lett.* **2013**, *103*, 173705.
- (29) Mei, Y.; Huang, G.; Solovev, A. A.; Ureña, E. B.; Mönch, I.; et al. *Adv. Mater.* **2008**, *20*, 4085–4090.
- (30) Ma, L.; Li, S.; Quiñones, V. A. B.; Yang, L.; Xi, W.; et al. *Adv. Mater.* **2013**, *25*, 2357–2361.
- (31) Smith, E. J.; Schulze, S.; Kiravittaya, S.; Mei, Y.; Sanchez, S.; et al. *Nano Lett.* **2010**, *11*, 4037–4042.
- (32) Smith, E. J.; Liu, Z.; Mei, Y.; Schmidt, O. G. *Nano Lett.* **2009**, *10*, 1–5.
- (33) Harazim, S. M.; Xi, W.; Schmidt, C. K.; Sanchez, S.; Schmidt, O. G. *J. Mater. Chem.* **2012**, *22*, 2878–2884.
- (34) Paguirigan, A. L.; Beebe, D. J. *Integr. Biol.* **2009**, *1*, 182–195.
- (35) Pitaval, A.; Tseng, Q.; Bornens, M.; Théry, M. *J. Cell Biol.* **2010**, *191*, 303–312.
- (36) Macville, M.; Schrock, E.; Padilla-Nash, H.; Keck, C.; Ghadimi, B. M.; et al. *Cancer Res.* **1999**, *59*, 141–150.
- (37) Hergott, G. J.; Sandig, M.; Kalnins, V. I. *Cell Motil. Cytoskeleton* **1989**, *13*, 83–93.
- (38) Thompson, S. L.; Compton, D. A. *Proc. Natl. Acad. Sci. U.S.A.* **2011**, *108*, 17974–17978.
- (39) Schwartzman, J.-M.; Sotillo, R.; Benezra, R. *Nat. Rev. Cancer* **2010**, *10*, 102–115.
- (40) Musacchio, A.; Salmon, E. D. *Nat. Rev. Mol. Cell Biol.* **2007**, *8*, 379–393.
- (41) Santaguida, S.; Tighe, A.; D'Alise, A. M.; Taylor, S. S.; Musacchio, A. *J. Cell Biol.* **2010**, *190*, 73–87.
- (42) Itabashi, T.; Terada, Y.; Kuwana, K.; Kan, T.; Shimoyama, I.; et al. *Proc. Natl. Acad. Sci. U.S.A.* **2012**, *109*, 7320–7325.
- (43) Dumont, S.; Mitchison, T. J. *Curr. Biol.* **2009**, *19*, 1086–1095.
- (44) Magidson, V.; O'Connell, C. B.; Loncarek, J.; Paul, R.; Mogilner, A.; et al. *Cell* **2011**, *146*, 555–567.
- (45) Brito, D. A.; Rieder, C. L. *Cell Motil. Cytoskeleton* **2009**, *66*, 437–447.
- (46) Matsusaka, T.; Pines, J. *J. Cell Biol.* **2004**, *166*, 507–516.
- (47) Hartwell, L.; Kastan, M. *Science* **1994**, *266*, 1821–1828.
- (48) Dalerba, P.; Kalisky, T.; Sahoo, D.; Rajendran, P. S.; Rothenberg, M. E.; et al. *Nat. Biotechnol.* **2011**, *29*, 1120–1127.
- (49) Smith, E. J.; Xi, W.; Makarov, D.; Monch, I.; Harazim, S.; et al. *Lab Chip* **2012**, *12*, 1917–1931.